Studies of Au clusters on a Graphene covered Ir(111) substrate: cluster growth and CO adsorption

Johan Knutsson

Division of Synchrotron Radiation Research

Department of Physics

Lund University

Sweden

9/13/2010

LUND UNIVERSITY

Studies of Au clusters on a Graphene covered Ir(111) substrate: cluster growth and CO adsorption

JOHAN KNUTSSON
JOHAN.KNUTSSON@GMAIL.COM

DIVISION OF SYNCHROTRON RADIATION RESEARCH
DEPARTMENT OF PHYSICS

Supervisors:
PROF. JESPER N ANDERSEN
AND PHD JAN KNUDSEN

September 29, 2010

LUND
UNIVERSITY

ABSTRACT

The chemical properties of 0.2-1 ML Au clusters have been studied using *X-ray photoelectron spectroscopy* (XPS). By exposing the clusters to CO, at 10^{-7} mbar, in periods of two minutes, while systematically increasing the cluster size, a correlation between cluster size and CO adsorption was found. Furthermore, the most probable adsorption sites on the Au cluster were identified.

The clusters were grown, using Ir seeding, on a Ir(111) crystal covered by a monolayer of Graphene. The Au growth sites on the Graphene surface have been studied using *low energy electron diffraction* (LEED). In addition, the Graphene lattice constant as well as the distance between the Au adsorption sites have been calculated using LEED images and known values of the Ir lattice constant as a reference.

Johan Knutsson

Guldklustrar- storleken har betydelse

Utveckling och framsteg inom material- och ytfysik har blivit allt viktigare för det moderna samhället. Snabbare och mindre datorer, bättre och effektivare ljuskällor, renare men effektivare energiprodktion. Listan på applikationer är lång och kraven många och hårda.

Således har det blivit allt viktigare att förstå material och dess ytors speciella egenskaper på en allt djupare nivå i takt med att kraven trappats upp. I dagsläget läggs mycket fokus på att försöka skräddarsy material på atomär nivå, så kallad *nanovetenskap*, d.v.s. att man försöker förstå vad varje atom och dess position har för betydelse för ett materials egenskaper.

Ytatomerna av material är av speciellt stort intresse då de ofta har egenskaper som skilljer sig från atomerna inuti det specifika materialet. Ytfysiken kan t.ex. svara på varför en vattendroppe rinner av en regnjacka men inte en bommulsjacka, eller varför järn rostar men inte rostfritt stål. Dessa ting kan tyckas vara vardagliga och triviala men svaret ligger alltså i hur atomerna är placerade och bundna till varandra.

Det krävs således mycket forskning, både grundläggande och tillämpad, inom detta område för att en genomgripande bild av den atomära världen och dess speciella lagar ska kunna kartläggas. Studierna inbegripna i det här kandidatprojektet försöker göra just detta genom att studera grundämnet guld. Guld är nämligen så gott som icke-reaktivt, och därför tämligen ointressant som kemisk reaktant under normala omständigheter i den makroskopiska världen.

Om man däremot tittar på atomär nivå och bildar små anhopningar av guldatomer, bestående av endast några dussin atomer, kommer dessa anhopningar plötsligt bli reaktiva. Kyler man sedan ner dessa blir den reaktiva effekten än mer potent. Det är alltså möjligt att göra ett tidigare oanvändbart material användbart inom ett visst område och således borde det även vara möjligt att förbättra redan användbara material.

För att kunna utnytja detta måste dock grundläggande studier göras för att förstå hur och varför detta sker. Fram tills nu har en mängd studier gjorts på guldklungor av varierande storlek och med många olika underlag. Underlaget i den här studien är en kristall av iridium med en viss ytstruktur benämnd som (111), vilket är täckt av ett kollager som endast är en kolatom tjockt, kallat Graphene.

Genom att utsätta guldklungorna för kolmonoxid (CO) i gasform under bestämda tidsperioder och tryck är det möjligt att bestämma reaktiviteten mellan guld och kolmonoxid. Anhopningarna gjordes sedan successivt större samtidigt som mätningar gjordes med hjälp av *röntgen-fotoelektron-spektroskopi* (XPS) för att kunna avgöra hur reaktiviteten förändrades med storleken på anhopningarna. På detta vis är det möjligt att få en klarare bild av storleksordningens betydelse i den atomära världen gällande metallanhopningars kemiska reaktivitet.

Examensarbete, Naturvetenskap, Lunds universitet

Kanditatprojektet innefattar även studier angående det använda underlag och den speciella superstruktur som bildas då Graphene läggs på en iridiumyta av (111)-typ. Dessa studier

gjordes med *lågenergetisk elektrondiffraktion* (LEED), vilket gjorde det möjligt att beräkna avståndet mellan atomerna i Graphene-lagret samt periodiciteten i superstrukturen som bildades.

Handledare: Prof. **Jesper N. Andersen** och PhD **Jan Knudsen**
Examensarbete 15 hp i fysik 2010
Fysiska institutionen, Avdelningen för synkrotronljusfysik, Lunds universitet

CONTENTS

1. INTRODUCTION

The demands on the industrial world have increased enormously in the last decade. Competition and pressure of technological development by the modern society have made it necessary to understand materials and their properties down to the atomic scale. Thus a lot of research and effort is put into this area of science. A large amount of the research is focused on surfaces and interfaces since they are an important part of almost any material. For instance, better understanding of protein mediation between cells membranes might lead to a revolution in viral and bacteria treatment. Other research has led to breakthroughs in areas such as corrosion protection, self cleaning and unscratchable windows as well as tailored catalytic substances. In other words, the broad area of applications has made surface science an important and interesting research field in recent years.

Understanding the fundamentals of atomic scale structures makes it possible to adapt, alter and shape the physical and chemical properties of those materials. Thus such knowledge can render non-usable materials usable for a specific area, and further enhance already useful materials. A good example is gold (Au) which until previously was believed to be totally inert, thus rendering Au useless as a chemical reactant or for instance a catalyst.

However, relatively recent studies [1] show that in small and ordered clusters, Au becomes chemically active. Understanding the properties of such metallic clusters, and why Au is made active, can thus prove to be useful in the development of new advanced catalytic materials.

The prime focus of this thesis is dedicated to investigate the chemical properties of such gold clusters. A major part also focuses on how to actually create small and ordered clusters of similar size. Although comparable studies have been made before [2, 3], using various different substrates, the Graphene covered Ir(111) crystal used as a substrate in my experiments might still give fundamental information on atomic scale systems. The Graphene layer was grown in order to induce a periodic variation in the electronic properties of the surface with preferred adsorption sites for the Au clusters.

These adsorption sites as well as the clean Ir(111) crystal and Graphene surface was studied using *low energy electron diffraction* (LEED). In addition, the Graphene lattice constant as well as the distance between the adsorption sites were calculated using known values of Ir lattice constants as reference.

The chemical properties of the Au clusters were investigated by exposing the Au clusters to gaseous CO molecules, at a chamber pressure of 10^{-7} mbar, for minute-long time periods. The clusters were studied with *X-ray photoelectron spectroscopy* (XPS) before and after CO exposure, in order to extract information regarding adsorption properties. By systematically increasing the cluster size, further information could be extracted regarding adsorption sites as well as correlations between relative cluster size and adsorption-efficiency.

In order to avoid contamination of the sample, other than by CO molecules, the experiments were conducted within a *ultra high vacuum* (UHV) environment. Although not being realistic as the operational environment of a catalyst, fundamental atomic scale information regarding properties of metallic clusters could still be extracted.

2. SURFACE STRUCTURES

The atomic arrangement in a perfect crystal is periodic in nature and can be considered as a lattice. The smallest periodicity of such a crystal can be represented by blocks of atoms, referred to as a *unit cell*. The relative position of the atoms is defined by three *base* vectors, $\mathbf{a}_1, \mathbf{a}_2$ and $\mathbf{a}_3$, which make up the base of the lattice. Regarding surfaces, only two base vectors are needed, as in fig. 2.3b.

Depending on the vector orientations several lattice configurations are possible, all put under the collective name of *Bravais* lattices. A Bravais lattice indicates the relative orientation of the lattice points in a crystal, and thus determines how each atomic layer is constructed. The most common lattice types, represented in fig. 2.1, are cubic in nature.

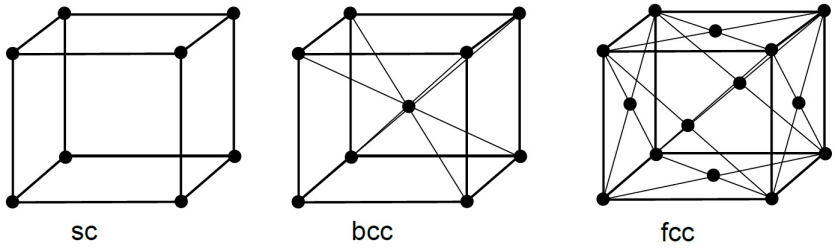

Fig. 2.1: The three most common *Bravais* lattices, all cubic in nature. The first one is refered to as *simple cubic* (sc), the second is *body centered cubic* (bcc) and the third is *face centered cubic* (fcc).

Different surface structures may be represented by cutting a certain Bravais lattice in different planes. The planes, and their respective lattice points, are defined by the three points whre the plane intercepts the x, y and z-axis. The distance from the origin, (000), to the interception points is measured in units of the *lattice constant* a, defined as the distance between two lattice points. Thus one can use the indexes (hkl), known as *Miller indices*, as a notation for a specific plane. Three such planes and their corresponding Miller indices are illustrated in fig. 2.2.

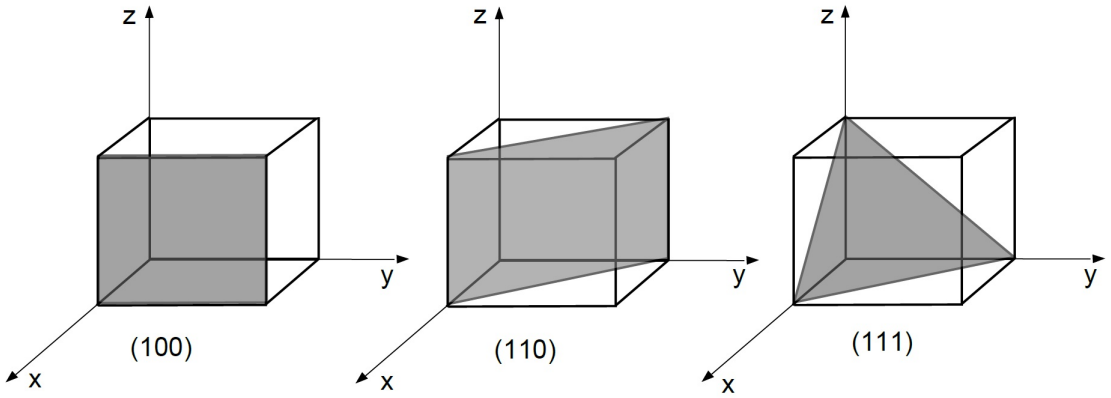

Fig. 2.2: Three common *low-index* planes for cubic lattice structures.

Depending on the Bravais lattice a certain plane will have a specific relative orientation of the surface points. The (111) plane of an fcc lattice will for instance have it's lattice points arranged in a hexagonal pattern, as in fig. 2.3. The surface, defined by the plane, can thus be represented by the two base vectors $\mathbf{a}_1$ and $\mathbf{a}_2$.

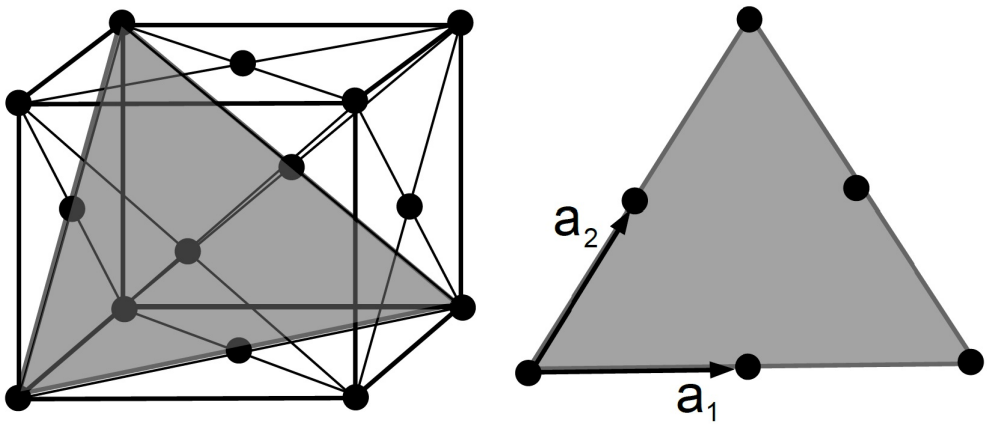

(a) The (111) plane of a fcc lattice.

(b) The corresponding surface, defined by the (111) plane.

Fig. 2.3: An illustration of how the surface of a (111) plane for a fcc lattice would look like. The surface will have it's lattice points arranged in a hexagonal pattern. Thus the surface plane can be represented by two base vectors $\mathbf{a}_1$ and $\mathbf{a}_2$.

The Bravais lattice of an Iridium crystal, the crystal used for the experiments included in this thesis, is fcc. The crystal was cut in a (111) plane, denoted as Ir(111), meaning that the arrangement of the surface atoms would be hexagonal. This is experimentally confirmed in section 4.

3. ULTRA HIGH VACUUM ENVIRONMENT

Experiments on surfaces are highly sensitive to unwanted contamination. Hence such experiments are conducted in clean and isolated environments. In order to keep the surface clean for a long enough period of time *ultra high vacuum* (UHV) is required. An estimation of the pressure, required to keep a sample clean for sufficient time periods, can be done by considering the number of particles per second and unit area R hitting the sample surface. If the sample is surrounded by gas molecules of mass M having a certain temperature T at a certain pressure P the impinging particle flux R can be estimated according to eq. 3.1 [4].

$$R \propto \frac{P}{\sqrt{MT}} \tag{3.1}$$

The relation suggests that a surface placed in a chamber at room temperature and with the pressure of 10^{-6} Torr, would be saturated within one second. This estimation assumes that all impinging particles are adsorbed. That assumption is however not realistic but can still be used to give a rough estimation of the pressure needed. The experimental pressure limit that defines UHV is $P_{UHV} \leq 10^{-9}$ Torr [5], but usual magnitudes are 10^{-10} to 10^{-11} Torr during actual experiments. These pressures can keep a sample clean for hours, in comparison to about 15 minutes for 10^{-9} Torr.

In order to achieve pressures as low as 10^{-11} Torr a series of pumping devices are needed. A *Roughing pump* in conjunction with a *Turbo pump* are used to usually reach pressures as low as 10^{-10} Torr. In order to reach lower pressures an *Ion pump* is used. A figurative description of the system can be seen in fig. 3.1.

The Roughing pump works according to fig. 3.2a. Gas is pumped out of the pumping chamber with each revolution of the pumping mechanism, resulting in a low pressure in the vicinity of the pump. The pressure from the experimental chamber then fills the pump again and the procedure is repeated. Thus it is obvious that the pumping process becomes ineffective at low pressures since the flow of particles into the pump is too low. The principle of the Turbo pump, see fig. 3.2b, solves this problem by accelerating the remaining particles towards the Roughing pump. This is achieved by letting them collide with rapidly rotating rotor blades. Thus, even if the mean free path is high, the remaining gas particles can be directed towards the Roughing pump and be pumped out of the system.

The final step is to use an Ion pump, seen in principle in fig. 3.2c. This pump ionizes the rest gas molecules by bombarding them with energetic electrons. The ionization results in charged gas particles, which are accelerated towards the cathode, due to a high voltage between anode and cathode. The cathodes are usually made of Titanium, which is highly reactive, and in the collision with the cathodes Titanium atoms are sputtered away. These are then adsorbed at various places in the pumping chamber, especially at the pumping envelopes which are plates located strategically according to fig. 3.2c. The colliding ionized gas particles are thus either absorbed by the Titanium cathodes or absorbed at Titanium rich locations, i.e the pumping envelopes.

This process slows down the saturation of the pumping envelopes remarkably since new Titanium is constantly adsorbed on the saturated layers due to the sputtering effect created by the ionized gas particles. The usage of Titanium, due to its reactivity, is very effective for reactive particles. On the other hand it's usefulness is very limited regarding inert gases, as for instance the noble gases. In those cases one has to rely on the fact that they can be mechanically buried instead of chemically bound, deep within the cathodes or envelope walls due to the strong acceleration, usually several thousand eV, induced by the anodes and cathodes.

In order to further increase the efficiency of the pump a strong magnetic field is applied. This induces a spiral movement of the ionizing electrons resulting in more collisions and thus making the pumping more effective. The principle of the ion pump does not allow it to actually pump the gas out of the system, but rather to bind it within it, which means that it will become saturated vary fast when used at higher pressures. Thus usual operating pressures are between 10^{-4} and 10^{-11} Torr [4].

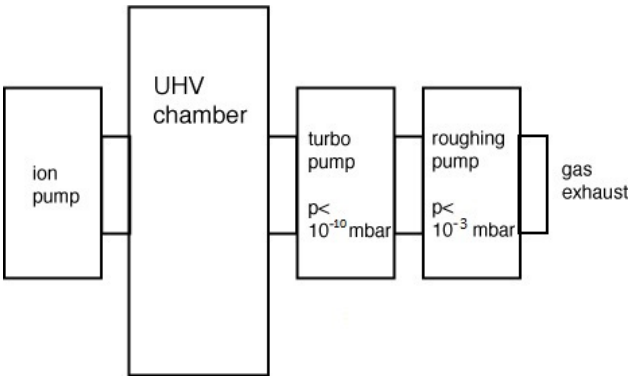

Fig. 3.1: Simplified schematic figure of the pumping system required in order to reach UHV. The Roughing pump and the Turbo pump represents in conjunction a pumping system, in which the gas is pumped out via the gas exhaust, able to reach down to pressures as low as 10^{-10} Torr. The ion pump is in itself a closed pumping system, i.e. it does not pump gas out of the chamber, it only binds it within, and thus no gas exhaust is needed. Figure taken from [4].

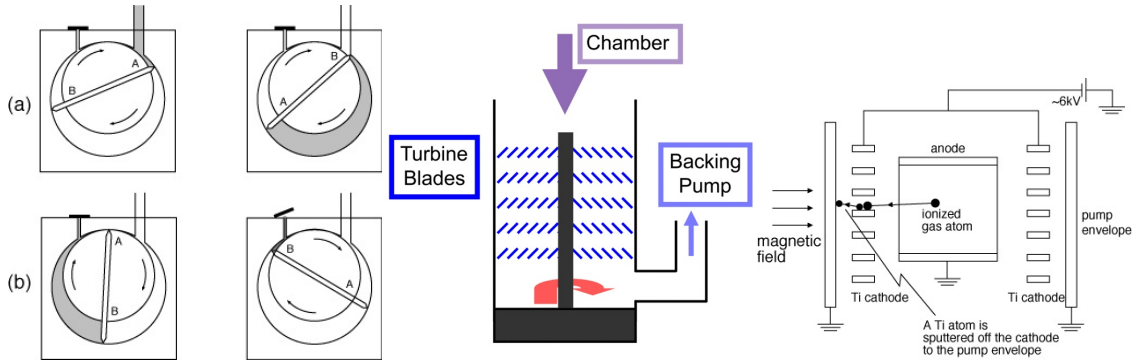

(a) Principle of roughing pump *(b)* schematics of a turbo pump *(c)* Schematics of an ion pump

Fig. 3.2: Fig. (a) represents the roughing pumps pumping mechanism, in which gas is constantly pushed out of the system. Due to pressure differences the pumping chamber is constantly refilled with gas from the experimental chamber as long as the pressure is high enough. When the mean free path is too high the pressure difference needed for the pumping process is negligible and the pump is thus ineffective. This is solved by connecting it to a Turbo pump, displayed in fig. (b), which accelerates the remaining particles towards the Rouging pump, thus making it effective even at low pressures. Fig. (c) displays a schematic figure of an Ion pump which in a chemical way binds the remaining particles within Titanium plates. Figures taken from [4].

Another important aspect in reaching UHV is the so called bakeout in which the whole system is heated to at least 400-500 K. During the bakeout, unwanted molecules attached, on or within, the walls of the chamber will desorb and can thus be pumped out. The bakeout process is one of the most time consuming parts in an experiment and is often done for a whole day, 24 hours [4].

3.1 Cleaning and preparing the sample

A common method used to clean polluted samples is to bombard them with ions (*sputter*), usually from noble gases i.e. Argon (Ar). The common usage of noble gases is based on the fact that they are very inert which is a desired property since the particles can be easily pumped out of the system again.

The sputtering principle is rather straightforward and and in good analogy to sandblasting. One simply shoots energetic ions, usually between 100-3000 eV [5], at the sample surface resulting in physical removal of unwanted molecules and atoms bound to the surface.

Unfortunately, the bombardment also distorts the surface, leaving a very rough surface. Experiments often rely on the sample surface being atomically flat. This poses a problem which is solved by annealing the crystal to temperatures corresponding to approximately $2/3$ of its melting point. This results in a reconfiguration of the surface atoms to a flat and ordered surface. This process also helps to desorb noble gas atoms, used for the sputtering, which penetrated the surface and became enclosed within the bulk during the sputtering process.

The sputtering and annealing process is often repeated a number of times in order to obtain an adequate smoothness of the sample surface for the specific experiment.

4. LOW ENERGY ELECTRON DIFFRACTION

Low energy electron diffraction (LEED) is a commonly used spectroscopic method utilized to obtain information about the overall periodicity of a surface. As the name implies the method is based on the diffraction phenomenon, which will give rise to interference. The interfering waves will result in pattern which is then used as a tool to analyze the surface periodicity. The theory is in analogy with the basic diffraction patterns formed when letting light pass through a number of slits or gratings, separated by a distance which roughly corresponds to the wavelength of the light, see fig. 4.1.

In LEED one utilizes the particle-wave duality, stated by L. de Broglie in 1924 [6], in which a particle is considered to have a wavelength λ according to eq. 4.1, where p is the momentum of the particle and h is Planck's constant.

$$\lambda = \frac{h}{p} \tag{4.1}$$

In this method low energy electrons, 10-1000 eV, are used since their wavelength approximately matches the distance between atoms in a solid. This is favorable since a beam of mono-energetic electrons is relatively easy to produce. Another advantage following from the fact that electrons are used instead of light is that this method is very surface sensitive. This origins from the fact that the mean free path of low energetic electrons in a solid is very low, approx. 5-20 Å [5]. As a result, the electrons will not penetrate more than only a few of the topmost atomic layers. Unfortunately this also means that one has to operate in UHV when doing LEED experiments, which makes the method a little more time consuming as well as increases the requirements on the equipment used.

4.1 Theoretical description and the reciprocal space

In order to interpret the diffraction pattern one must have a basic understanding of the *reciprocal space*[1]. This is vital for LEED experiments since the lattice of the sample is in real space while the diffraction pattern is in reciprocal space. Thus in order to deduce information about the real space lattice, one must understand its relation to the reciprocal lattice displayed in a LEED diffraction pattern.

The real space base vectors $\mathbf{a}_1$ and $\mathbf{a}_2$ can be used to construct a general lattice vector $\mathbf{R}$ using two constants m_1 and m_1 (see fig. 4.2a) so that:

$$\mathbf{R} = m_1\mathbf{a}_1 + m_2\mathbf{a}_2 \quad ; m_1, m_2 = \pm 0, 1, 2, 3 \ldots \tag{4.2}$$

The next step is to consider an incident beam of electrons with a specific wave vector $\mathbf{k}$ which when scattered at two surface atoms, related by $\mathbf{R}$, gains a new wave vector $\mathbf{k}'$, as in fig. 4.3. Lets also assume that the scattering is elastic, meaning that no energy is lost in the collision, so that $|\mathbf{k}| = |\mathbf{k}'| = k = \frac{2\pi}{\lambda}$.

In order to get constructive interference the two waves must be in phase and thus the path difference, $PD = s + s'$, must be a multiple of the wavelength: $PD = n\lambda = n\frac{2\pi}{k}$. Thus the expression in eq. 4.3 below can be created if one defines $\Delta\mathbf{k}$ as $\Delta\mathbf{k} = \mathbf{k}' - \mathbf{k}$.

$$\mathbf{R}\Delta\mathbf{k} = 2\pi n \tag{4.3}$$

Equation 4.3 should be fulfilled for all lattice vectors $\mathbf{R}$ in order to get constructive interference. If this is the case $\Delta\mathbf{k}$ defines a *reciprocal* lattice vector, denoted as $\mathbf{G}$. $\mathbf{G}$ is composed by two reciprocal base vectors, $\mathbf{a}_1^*$ and $\mathbf{a}_2^*$, as in eq. 4.4. In this equation q_1 and q_2 are integers.

[1] a.k.a. *k-space* since the dimensions are made up by wavenumber-vectors, which are denoted by the letter k.

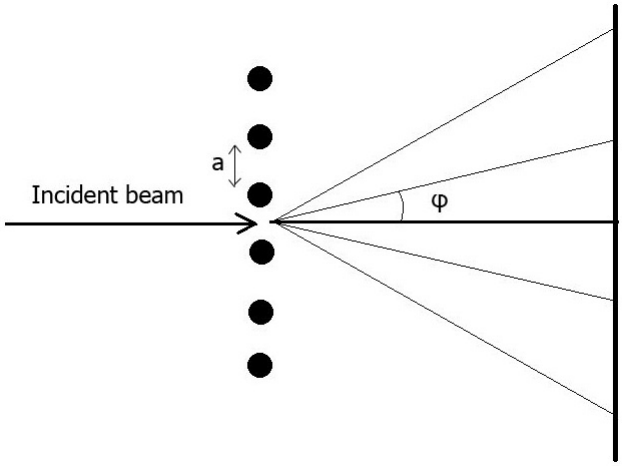

Fig. 4.1: Basic figure describing the diffraction phenomena, which results in constructive interference for certain values of the angle φ . The black dots represents a lattice with the lattice constant a. The relation between the angle, wavelength and lattice constant is: $asin(\varphi) = n\lambda$.

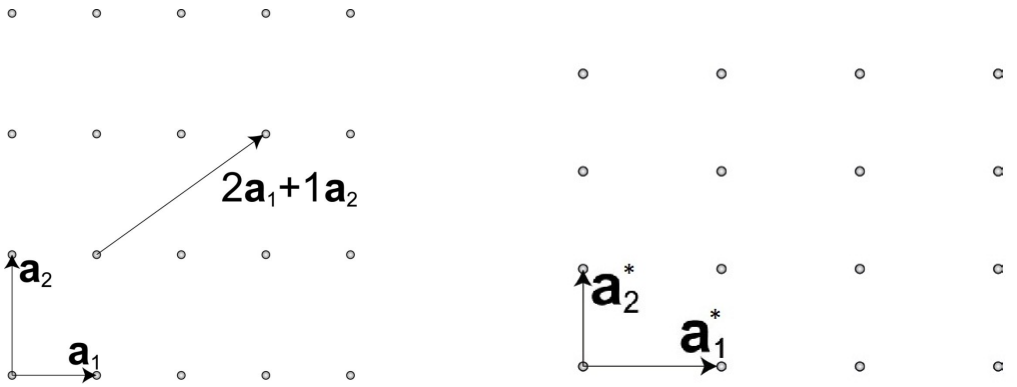

(a) Real space base vectors *(b)* Reciprocal space base vectors

Fig. 4.2: Figure a. represents a two dimensional real space lattice with the lattice base vectors $\mathbf{a}_1$ and $\mathbf{a}_2$ which when multiplied by integer numbers m_1 and m_2 creates a vector $\mathbf{R}$ which can be connected to at all lattice sites. Figure b. displays the corresponding reciprocal lattice with its reciprocal lattice vectors $\mathbf{a}_1^*$ and $\mathbf{a}_2^*$. The two lattices are identical but rotated 90° with respect to each other. Both figures taken with concent from [7]

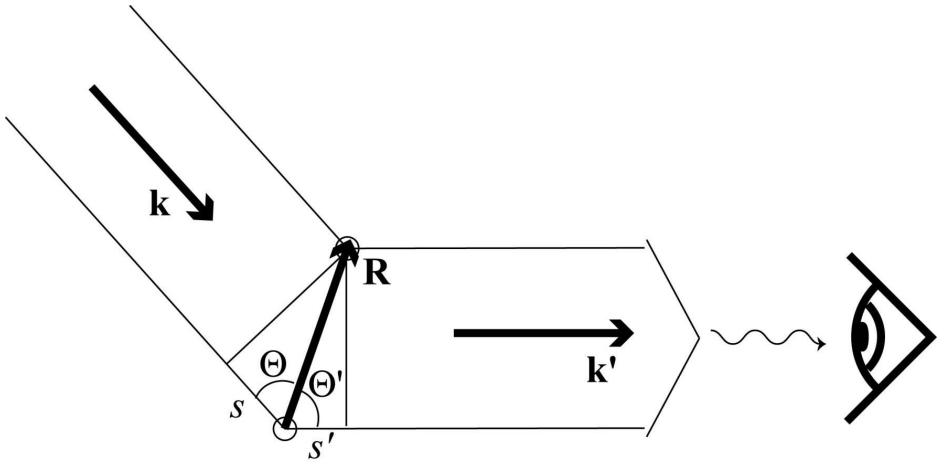

Fig. 4.3: Figurative description of elastic scattering in a lattice and $|\mathbf{R}|$ represents the length of the lattice constant if $\mathbf{R}$ is a lattice vector pointing from one atom to another. The incident particles with the wave vector $\mathbf{k}$ scatters elastically on the atoms, resulting in a new wave vector $\mathbf{k}'$. The path difference, PD, between the two outgoing waves is represented by $PD = s + s'$, which must be equal to an integer number times the wavelength in order for constructive interference to occur. The angles Θ and Θ'represent the incident angle between the vector $\mathbf{R}$ and the incident and scattered waves respectively. Figure taken with consent from [7].

$$\mathbf{G} = q_1\mathbf{a}_1^* + q_2\mathbf{a}_2^* \tag{4.4}$$

The relation between the reciprocal base vectors and the real space base vectors is such that $\mathbf{a}_i\mathbf{a}_j^* = \delta_{ij}2\pi$. As a result, $\mathbf{a}_1$ and $\mathbf{a}_2^*$ are perpendicular to each other, which of course also applies to $\mathbf{a}_2$ and $\mathbf{a}_1^*$. This is illustrated in fig. 4.2. This means that $\mathbf{a}_i\mathbf{a}_i^* = 2\pi$, which can be expressed as in eq. 4.5 below.

$$\mathbf{a}_i^* = \frac{2\pi}{\mathbf{a}_i} \tag{4.5}$$

This equation reveals that the dimension of the reciprocal space is inverse meter, m^{-1}. A consequence of this is that large distances in real space will be represented by small distances in reciprocal space, and vice versa. Another consequence is that for two dimensions the reciprocal lattice is rotated 90° with respect to the real space lattice, see fig. 4.2.

4.2 Experimental setup

A mono-energetic electron beam is created by heating a filament. The beam is then focused onto the sample surface. The potential difference between the sample and the filament defines the kinetic energy of the electrons, ranging from 10-1000 eV [5]. The inbound electrons will be backscattered, both elastically and inelastically. Constructive interference due to the scattering will occur for quantized angles corresponding to previously discussed conditions. The incident beam, with the wave vector $\mathbf{k}_i = \mathbf{k}_{i\perp} + \mathbf{k}_{i||}$, will have momentum components which are both parallel and perpendicular to the surface. It is however only of interest to know the momentum exchange parallel to the surface for the scattered electrons.

Thus for two dimensions, i.e. a surface, the condition for constructive interference stating that $\Delta\mathbf{k}$ has to correspond to a reciprocal vector $\mathbf{G}$ may be edited so that only the component parallel to the surface has to fulfill the criterion: $\mathbf{G}_{||} = \Delta\mathbf{k}'_{i||}$.

By placing a fluorescent hemispheric screen in front of the surface, but behind the electron gun as in fig. 4.4a, light will be emitted when electrons hit the fluorescent screen. Thus, for discrete angles bright dots will appear due to constructive interference. Viewing the screen from above, see fig. 4.4b, will reveal a periodic pattern of dots which represents the reciprocal lattice of the sample surface.

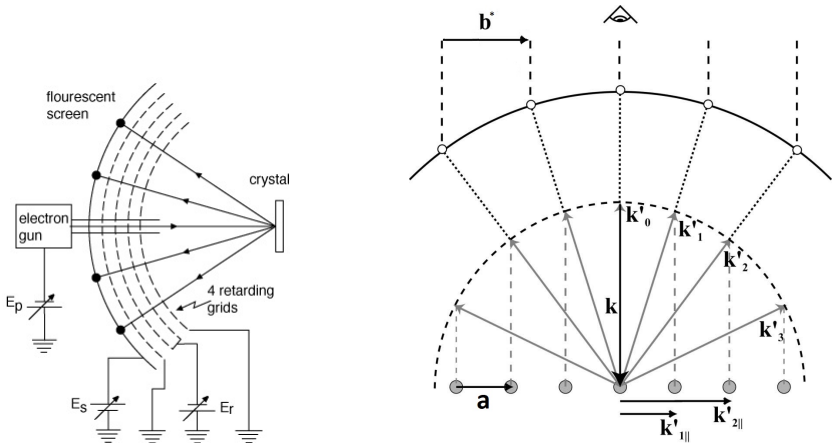

(a) Schematic figure of a LEED experimental setup.

(b) Illustration of how the LEED pattern occurs.

Fig. 4.4: Figure (a), taken from [4], displays a Schematic figure of a standard setup for a LEED experiment. An electron gun shoots a beam of electrons onto the crystal target on which they are scattered into different directions. For some specific angles, depending on the lattice structure of the sample, constructive interference will occur. At those angles bright spots will appear at the hemispherical florescent screen. The location of the spots is thus related to the structure of the surface. The four retarding grids are used to make sure that only the elastically scattered electrons reach the screen, and thus retard the inelastically scattered electrons enough so that they don't reach the screen. Figure b. explains how the scattered electrons with discrete wave vectors $\mathbf{k}_i'$ will give rise to constructive interference and when projected on a hemispherical florescent screen will represent the reciprocal lattice. Image taken from [7]

Since only the elastically scattered electrons are of interest a number of retarding grids are placed in front of the fluorescent screen, illustrated in fig. 4.4a. The inelastically scattered electrons are filtered out by applying a negative bias (E_r). The outermost and innermost grids are grounded and placed there to make sure that all electrons travel in a field-free environment. The fluorescent screen itself has a positive bias applied to accelerate, the now retarded, elastically scattered electrons that just made it through the filtering grids to energies required to cause light emission [5].

A drawback of LEED is that the sample material must be conducting and grounded in order to prevent charge from building up on the sample surface. In addition, the surface atoms must be configured in a periodic fashion.

4.3 Data and analysis

LEED experiments were conducted on a clean Ir(111) crystal before and after the deposition of a Graphene layer[2], i.e. a carbon film. This section is divided into two parts, one concerning only the clean Ir(111) surface and one in which the Graphene layer has been grown. All LEED images were taken using the same apparatus and settings, and with an electron energy of 79.2 eV.

4.3.1 The clean Ir(111) crystal

The pattern in fig. 4.5a reveals a hexagonal lattice structure for Ir(111). The reciprocal lattice vectors are defined as eq. 4.6:

$$\mathbf{G}_{Ir} = q_1\mathbf{a}_1^* + q_2\mathbf{a}_2^* \quad ; q_1, q_2 = \pm 0, 1, 2, 3 \ldots \tag{4.6}$$

The "length" of these vectors are both the same, meaning that $|\mathbf{a}_1^*| = |\mathbf{a}_2^*| = a^*$. Thus this should also apply to the real space equivalence of these vectors, $\mathbf{a}_1$ and $\mathbf{a}_2$, so that $|\mathbf{a}_1| = |\mathbf{a}_2| = a$. Experimental values of a were determined

[2] The preparation of the crystal, including the growth of the Graphene layer, is explained in detail in section 5.2

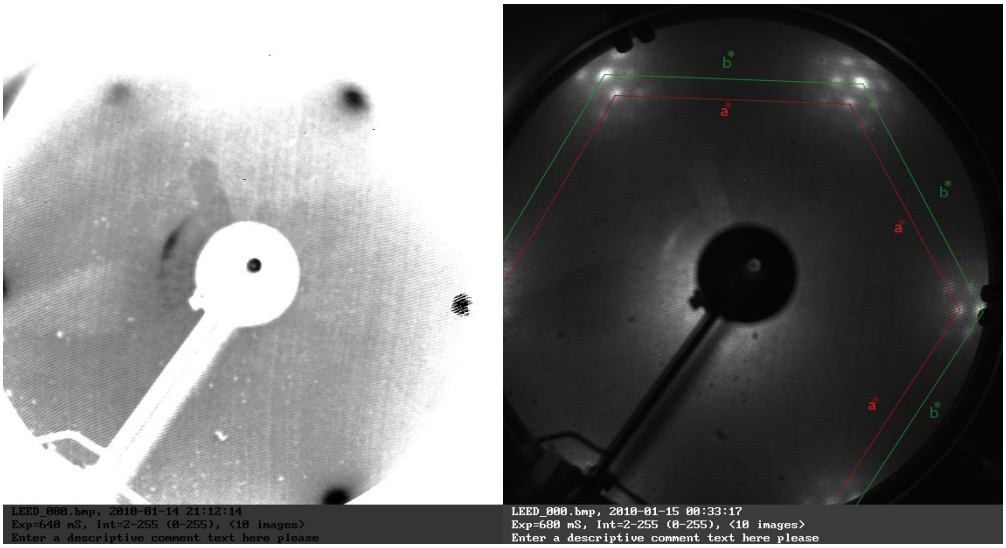

(a) Clean Ir(111) crystal *(b)* Ir(111) crystal with one layer of Graphene

Fig. 4.5: The figures displays a LEED pattern obtained when shooting electrons with energy 79.2 eV on a Ir(111) surface before and after the growth of a Graphene layer. The contrast in figure (a) has been inverted in order to highlight the spots. The Green lines in figure (b) represent the carbon hexagon structure, and the red lines represent the iridium structure. a and b represent the lattice parameters in reciprocal space. Other dots are part of a moire structure.

to be $a = 2.715$ Å according to measurements done by N'Diaye et al. in [8]. This value will be used as a reference in order to convert vector length in the LEED images from pixels to Å.

4.3.2 Ir(111) crystal with Graphene

According to the LEED pattern in fig. 4.5b the Graphene layer also has a hexagonal lattice structure. Thus it will have lattice vectors according to eq. 4.7 so that $|\mathbf{b}_1^*| = |\mathbf{b}_2^*| = b^*$. The Graphene lattice points were identified as the most intense ones in the image. The most remarkable difference, in comparison to the clean Ir(111) crystal image, is that this image has a rosette-like pattern around each Graphene spot. This rosette like structure is a fingerprint of a *moiré* structure, a common effect when two lattices with slightly different lattice constants are superimposed on each other. The origin of this effect is discussed in detail in section 4.3.3 below.

$$\mathbf{G}_C = q_3\mathbf{b}_1^* + q_4\mathbf{b}_2^* \quad ; q_3, q_4 = \pm 0, 1, 2, 3 \ldots \tag{4.7}$$

In fig. 4.5b one can also identify the Ir(111) hexagonal lattice by superimposing the pattern from fig. 4.5a on the pattern in fig. 4.5b. Both lattice structures are marked out in figure. Identifying both structures makes it possible to determine their relative size and thus also the coverage of carbon atoms on the iridium surface. From fig. 4.5b the length of the lattice constants a^* and b^* were determined to be 266 pix. and 294 pix. respectively. According to the calculations in eq. 4.8 below this gives a ratio of about 10:9.

$$\frac{b^*}{a^*} = \frac{294}{266} = 1.105 \approx \frac{10}{9} \tag{4.8}$$

Considering that this ratio applies to reciprocal space, thus $10a^* = 9b^*$, it must be inverted in order to apply to real space. Hence $9a = 10b$, meaning that on a square filled with 9×9 Ir atoms one can fit 10×10 carbon atoms. By using the value 2.715 Å for a, obtained from [8], in the ratio calculation it is possible to estimate the length of the Graphene lattice constant. Doing so suggested a vector length of b to be approximately $b = \frac{1}{1.105}a \approx 2.46 \pm 0.03$ Å.

By superimposing the Ir(111) LEED image on the Graphene/Ir(111) image it is also possible to deduce if the Graphene layer is rotated with respect to the Iridium structure, and if so calculate an approximate angle. If their lattice

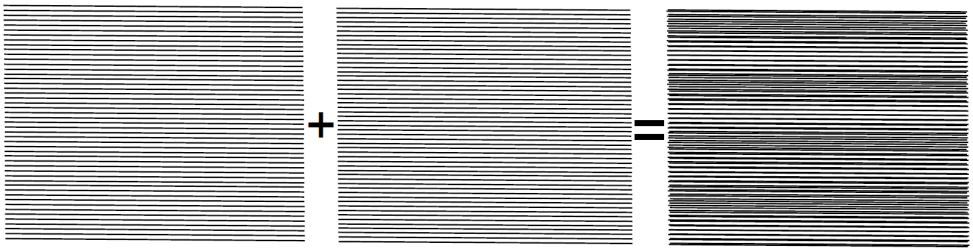

Fig. 4.6: An illustrative way of explaining what a moiré pattern is. Two lattices with slightly different lattice constants are superimposed on each other, inducing a new larger periodicity referred to as a moiré pattern.

structures were rotated with respect to each other in real space they would be rotated with the same angle in reciprocal space. This is not observed in fig. 4.5b indicating an aligned overlayer structure.

4.3.3 Origin of the moiré pattern

The rosette patterns in fig. 4.5b is present since the lattice constant of Ir(111) and Graphene are slightly different. When superimposing two such lattices, a large periodicity will appear, referred to as a *moiré* pattern. Figure 4.6 illustrates this effect rather clearly. This new periodicity can be considered as a lattice, also known as a *super lattice*, having a reciprocal vector $\mathbf{G}_{C/Ir}$ consisting of the bases of Ir(111) and Graphene as in eq. 4.9. Since it can be considered as a lattice, it will give rise to a diffraction pattern in the same way as the atomic lattice structures. The distances between the spots representing the moiré pattern in fig. 4.5b is rather small, in comparison to the Ir or Graphene lattice points. This suggests that the corresponding real space periodicity is very large relative to the periodicity of Ir and Graphene.

$$\mathbf{G}_{C/Ir} = \overbrace{q_1\mathbf{a}_1^* + q_2\mathbf{a}_2^*}^{Ir} + \overbrace{q_3\mathbf{b}_1^* + q_4\mathbf{b}_2^*}^{Graphene} \tag{4.9}$$

From fig. 4.5b it becomes clear that also the moiré lattice is hexagonal since the rosette pattern displays a hexagonal shape. It also seems to be aligned with the atomic rows of the substrate and adsorbate atoms. The structure being hexagonal is not very surprising since both the Ir(111) surface and the Graphene layer has a hexagonal atomic lattice geometry.

A mathematical approach to understanding why the moiré pattern looks like it does would be to use the fact that it is constructed by the base vectors of both Ir(111) and Graphene, as in eq. 4.9. Thus one should be able to reconstruct the pattern using these vectors. This is done in fig. 4.7 which represents one of the rosette patterns from the LEED image. The coordinates x and y represent the directions of the vectors $\mathbf{a}_1^*, \mathbf{b}_1^*$ and $\mathbf{a}_2^*, \mathbf{b}_2^*$ respectively. The big spot in the middle represents a Graphene diffraction spot of the first order. The small spots represent the pattern caused by the moiré structure. Each location of a moiré spot is determined by selecting a specific combination of the integers (q_1, q_2, q_3, q_4) from eq. 4.9 such that the reciprocal lattice vector $\mathbf{G}_{C/Ir}$ represents a moir$\acute{e}$ spot.

The reason to why even more spots can be seen in the real LEED image is that one could of course use larger values for the integers $q_1, ..., q_4$. The dashed spot in fig. 4.7 was for instance created using the integers (-2020), thus giving rise to a *second order* spot. Considering this, there should be an infinite amount of spots. But since the spot intensity is gradually decreasing wit increasing magnitude of the integers $q_1, ..., q_4$ these will not be detected, except for a few of the second order.

The size of the real space moiré lattice structure can be determined quite easily using eq. 4.9 where the reciprocal lattice vector $\mathbf{G}_{C/Ir}$ represents the distance between two moiré maxima. Thus its length in reciprocal space would be for instance: $\left|\mathbf{G}_{C/Ir}\right| = |-1\mathbf{a}_1^* + 0\mathbf{a}_2^* + 1\mathbf{b}_1^* + 0\mathbf{b}_2^*| = |\mathbf{b}_1^* - \mathbf{a}_1^*| \approx 0.039$ Å^{-1} for the spot (010-1). Thus in real space the period of the moire structure would be approx. 26 ± 4 Å.

Another possibility is to measure the distance between two moiré spots in the LEED image and make a calculation similar to the one in eq. 4.8. Such a measurement gave a reciprocal moiré lattice length of $p^* = 29pix.$. Using the given value for Ir(111) as reference, as before, results in a moiré lattice constant value according to: $\frac{a^*}{p^*} = \frac{266}{29}a = 25 \pm 2$ Å.

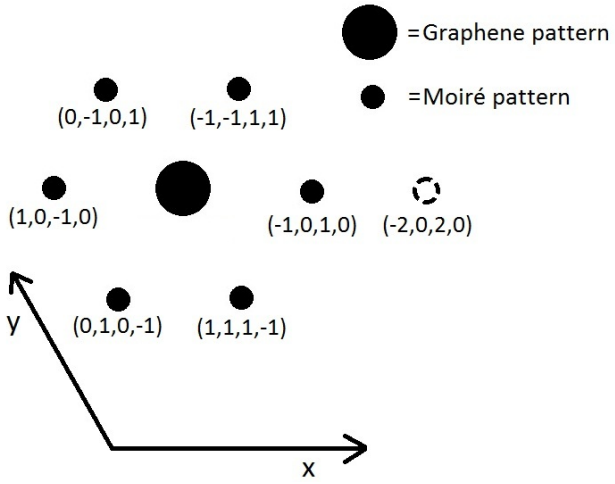

Figure 4.7: A reconstruction of the rosette pattern seen in the LEED images using the reciprocal base vectors $\mathbf{a}_1^*$, $\mathbf{a}_2^*$, $\mathbf{b}_1^*$ and $\mathbf{b}_2^*$ and given values of the integers (q_1, q_2, q_3, q_4), so that the reciprocal vector $\mathbf{G}_{C/Ir} = q_1\mathbf{a}_1^* + q_2\mathbf{a}_2^* + q_3\mathbf{b}_1^* + q_4\mathbf{b}_2^*$ gives the positions of the moiré spots. The x and y axis indicate the direction of the $\mathbf{a}_1^*$, $\mathbf{b}_1^*$ and $\mathbf{a}_2^*$, $\mathbf{b}_2^*$ respectively. The dashed spot indicates the would be position of a second order moiré spot which has a lower intensity.

These estimations of the moiré lattice constant correspond well to those in [8, 9, 10] since their calculations indicated that the lattice constant should be 25.8 ± 2 Å. STM images from [8, 9, 10] as well as [11] indicated that the moire symmetry domains had a varying heights, giving the Graphene surface a wave-like structure. See fig. 5.1b for illustration. This phenomenon is in good analogy to trying to fit a large paper on top a smaller paper. The result will be that the topmost paper will curve up into a wave pattern. According to the research done in [8, 9, 10, 11] the valleys are favorable sites for cluster growth.

4.4 Results from LEED

The LEED patterns showed that both the Ir(111) and the Graphene surface had a hexagonal lattice structure, although with slightly different lengths of the unit cell base vectors. The result was a rosette like moiré pattern which should be interpreted as a super lattice. Due to the super lattice the degree of symmetry varies along the surface giving rise to interesting binding properties at certain sites.

The determination of the Graphene lattice parameters b was done using the known Ir(111) parameters as reference. Utilizing the ratio between the Graphene structure and the Ir(111) structure in in the LEED image, the value $b = 2.46 \pm 0.03$ Å was obtained. This value corresponds rather well to the experimental values from [8] in which the parameters were determined to be 2.47 ± 0.02 Å.

The periodicity of the moiré unit cell was determined, in analogy to the Graphene cell, to be 26 ± 4 Å using vector calculations and 25 ± 2 Å using ratio calculations with Ir(111) as reference. These values correspond rather well to the experimental values in [8, 9, 10] in which the periodicity was estimated to be 25.8 ± 2 Å.

Furthermore, no rotation between the lattices of the substrate Ir(111) surface and the Graphene layer could be noticed.

5. X-RAY PHOTOELECTRON SPECTROSCOPY

X-ray photoelectron spectroscopy (XPS) is a commonly used method to determine the energies of the occupied electronic states in an atom, molecule or surface. The basic principle is to shoot photons onto a sample which thus will emit electrons of energies related to the electronic state it originated from. The energy of these electrons are then measured and analyzed. The principle thus relies on the photoelectric effect, first observed by Heinrich Hertz in 1887 [12]. Later in 1921 Albert Einstein was awarded the Noble prize for his explanation of the phenomenon in 1905 [13].

The principle states that atomic electrons can absorb photons of energies $h\upsilon$, resulting in excitations of the electron. Photon energies larger than the electronic state binding energy (BE) E_{BE} will result in an ejection of the electron into the vacuum level. Here it will be *free*, with a kinetic energy E_{kin}.

In XPS the kinetic energy distribution of the emitted electron is measured, using an energy analyzer [1], and due to energy conservation the binding energies E_{BE} of the occupied atomic or molecular orbitals can be determined (see eq. 5.1):

$$E_{BE} = h\upsilon - E_{kin} \tag{5.1}$$

Monochromatic light is required for the relation to be useful in practice. The relation in eq. 5.1 further indicates that the degree of monochromatization in conjunction with the resolution of the energy analyzer determines the total energy resolution of an experiment.

XPS is surface sensitive and it is thus perfect for investigating surfaces. The surface sensitivity originates from the short mean free path of an electron in matter.Although the actual photons can penetrate deep into the sample without loosing much intensity, the majority of the photoelectrons from the bulk will quickly be scattered inelastically and loose energy. The energy losses is due to for instance excitation of atomic electrons or plasmons. The photoelectrons from the surface layers will however not experience inelastic scattering to the same extent as the bulk, since their path through matter is much smaller.

The scattered bulk electrons that actually reach the detector gives rise to the background intensity present in most measurements. The shape of the background is dependent on the probability distribution for electrons with a given kinetic energy to undergo inelastic scattering.

Surface and bulk atoms will differ slightly in BE due to different chemical environments. The energy difference is commonly referred to as a *chemical shift* and makes it possible to identify specific molecular species. This phenomenon indicates that the experiment must be conducted in UHV in order to avoid contamination, which would result in numerous unwanted chemical shifts.

The BE scale must be fixed in order for results to be comparable. This is solved by defining the BE scale with respect to the highest occupied electronic state, denoted as the *Fermi level*. Thus a measurement of the Fermi edge is taken in conjunction with every spectrum in order calibrate the energy scale. The Fermi edge is defined as zero BE.

In order to avoid charging due to the created electron *holes*[2], the sample is grounded via an electrical connection to the energy analyzer.

5.1 Experimental setup

The experiments were conducted at beam line I311 of the synchrotron radiation facility MAX-lab in Lund. The light source used was thus synchrotron radiation from continuously accelerated electrons, emitting photons in the soft X-ray region. By letting the light scatter from a grating it will be spread angularly. The angle is directly related to the

[1] see sec. 5.1

[2] An absent electron in a specific orbital may be considered, since electrons are negatively charged, as a positive charge referred to as an electron *hole*.

wavelength, and thus the energy, of the photons. Thus a single well defined wavelength could be picked out by using a slit. The width of the slit determine the energy interval of the photon energy in addition to the intensity of the photon beam.

Using a series of focusing mirrors it is possible to optimize the beam intensity and focus the beam onto the sample, placed within the experimental chamber. When the X-rays are incident on the sample (photo)electrons are emitted due to photoemission. The kinetic energy of the electrons are measured using an energy analyzer, which in principle is two hemispherical plates placed on top of each other.A potential difference between the plates will change the trajectory of the electron, making it bend. The degree of bending is related to the kinetic energy of the incoming electron. Thus only electrons with a specific energy will pass through the whole analyzer and to the detector, while the others will hit either the outer or inner walls depending on the energy. The specific electron energy required to reach the detector is called the *pass energy* and is held constant. By applying a potential difference between the sample and the energy analyzer, and alter its strength, it is possible to increase or decrease the energy of the inbound electrons so that it matches the *pass energy*. Thus it is possible to create an electron energy spectrum by *scanning* the electron energies and measure the number of electrons reaching the detector.

5.2 Preparing a sample

The experiments described in this paper utilizes an Ir(111) substrate on which a Graphene film is grown. On top of this, Au clusters are deposited.

The first step in preparing the sample is a routine cleaning process, as described in section 3.1, followed by a LEED experiment in order to determine the surface quality. If sufficient, the Graphene film is grown and the quality is again checked with LEED as described in the following section. The whole procedure is conducted within a preparation chamber, sealed of from the experimental chamber in order to keep it from being contaminated.

5.2.1 Growing the Graphene film

The Graphene film is grown using Ethylene, C_2H_4. Exposing the Ir crystal to gas phase ethylene at room temperature results in a saturation of the surface. The electronic properties of the Ethylene restricts the growth to one ML [14, 15]. Heating the sample to Graphene growth temperatures, around 1200 K, induces a desorption of the weakly bonded hydrogen atoms. The remnant carbon atoms reorganize and form Graphene in small cluster-like islands. All island lattice vectors are aligned with respect to each other, and also to the substrate.

Studies [14] show that Graphene domains exposed to Ethylene at elevated temperatures induce further growth of the islands with the same orientation. Hence by doing so, the Graphene islands could be grown to cover the entire substrate surface. The result would be a fully aligned Graphene film covering the whole substrate surface. The Graphene growth process takes approximately 20 min, and is followed by a LEED experiment in order to deduce the quality of the film.

5.3 Creating the Au clusters

The gold atoms are deposited by twisting a small Au wire around a tungsten (W) rod and placing it in the close vicinity of the sample surface. The Au-wire is heated, resulting in Au sublimation onto the sample.

The Au coverage is regulated by varying the Au exposure time, and in order to be consistent the same Au vaporing pressure must be used for all dosing instances. In addition, a calibration is done in order to correlate the Au sublimation-time to the Au coverage on the surface.

In order to create clusters of roughly the same size, Ir atoms were seeded onto the surface in clusters of only a few atoms. The Ir atoms will bind to the hcp-regions of the Graphene moiré lattice, see fig. 5.1. Hcp refers to *hexagonal close packed*. Deposited Au atoms will then bind to the seeded Ir atoms, resulting in the creation of Au clusters on top of a small Ir cluster. The Au atoms will totally cover the seeded Ir atoms, a fact known since no CO was present at room temperature after CO deposition. Since CO will bind to Au for only extremely short time periods at room temperature, which however not is the case for Ir, this means that no Ir atoms were exposed enough for a CO molecule to bind with it.

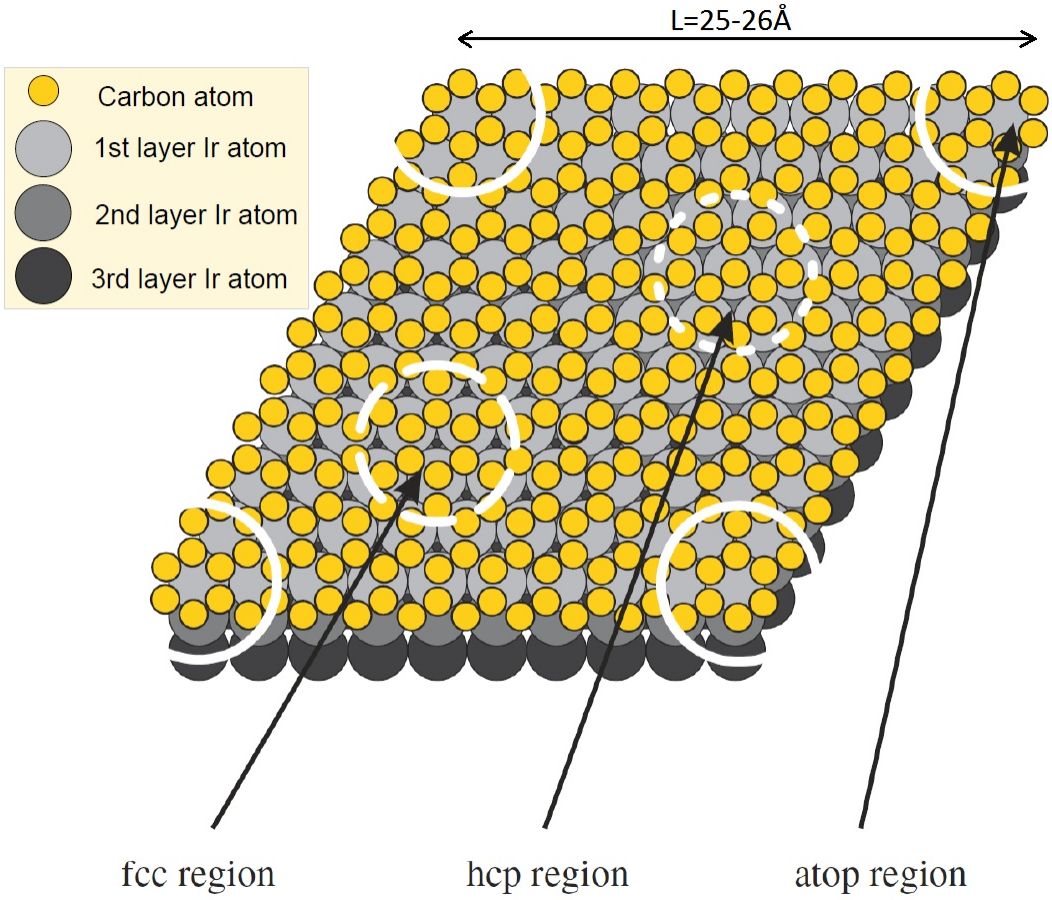

(a) The moiré super structure unit cell

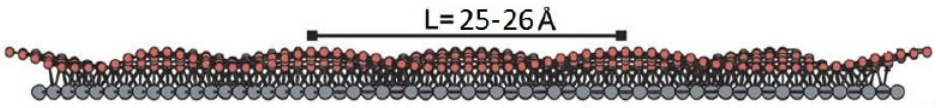

(b) Side view of the structure

Fig. 5.1: Figure (a) illustrates the moiré super structure unit cell. Three different regions are prominent, all having different arrangements of the overlaying carbon atoms with respect to the underlaying iridium atoms. The three regions are labeled: atop- fcc- and hcp-region. Hcp refers to: "*hexagonal close packed*". In the atop region, the carbon hexagonal structure is centered precisely on top of an underlying iridium atom. Totally covering the threefold coordinated sites. Both the fcc and hcp sites have a threefold coordinated site in the center of the hexagonal carbon structure. The distance between two sites of the same kind is roughly 25-26 Å according to estimations done in section 4. The image is taken, and edited, from [8]. Figure (b) displays a side view the Ir/Graphene structure, illustrating that the different sites vary in hight. A phenomenon which originates in that the length of the lattice vector for Ir and Graphene differs slightly. In this figure, the red balls represent the carbon atoms. Experiments indicate that the Au clusters grow at the hcp-sites only, which are located in the "valleys" of the wave-structure. The image is taken, and edited, from [11].

(a) Layer by layer growth.

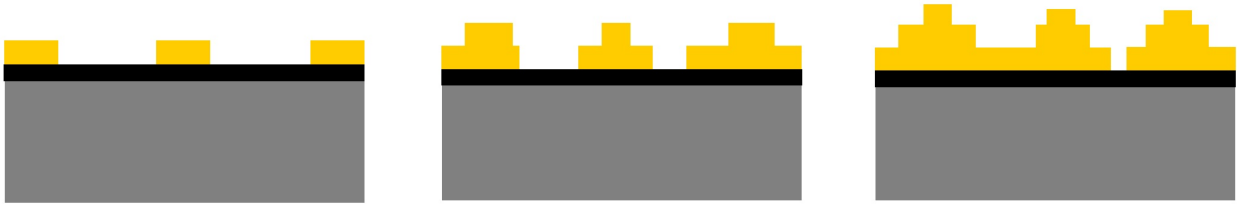

(b) Stepwise growth

Fig. 5.2: The figure illustrates two possible growth procedures for the Au cluster. Figure (a) describes a layer by layer growth process in which the second layer does not start to form until the first one is finished. Figure (b) illustrates a *stepwise* growth in which several layers are possible even at low coverages. On the other hand the whole surface will not be covered.

The formed clusters are separated by approximately 25-26 Å, see section 4, and constructed out of 1-2 (possibly 3) atomic layers depending on the Au coverage.Thus several formations and growth procedures are possible. See fig. 5.2 for further explanation. The presence of a bulk component[3] at even small Au coverages suggests that the *stepwise* growth process is the most probable, since the layer by layer approach does not allow for *bulk* atoms at low coverages.

5.3.1 Au calibration

The most convenient way to do the calibration would have been to use *Scanning Tunneling Microscopy*[4] (STM), but no such apparatus was available.

Another possible way utilizes the chemical shift of the Ir surface component due to the new chemical environment induced by the adsorption of Au atoms. When the substrate surface is partially covered with Au there should be two surface components at different binding energies, one for the clean parts and one for the Au covered parts. The intensity relation between the two components is directly associated with the Au coverage of the surface. This however requires that the binding energy shift between the surface peaks is large enough to resolve, as in the case of for instance Platinum (Pt) deposition. It also requires the Au islands to be only one atomic layer thick since more layers would give rise to additional components, making it hard to estimate the intensity ratios. Unfortunately the effect of the Au adsorption was too small to induce large enough shifts of the Ir surface component for this method to be easily applicable, see fig. 5.3.

The final method used proved to be more suitable. The Ir surface peak intensity of a clean Ir substrate was measured. The intensity should correspond to precisely one ML coverage. Au was then deposited a number of times at various deposition times. The Au peak intensity was measured at these deposition times and put in relation to the intensity of the Ir surface peak. An Au intensity corresponding to that of the Ir peak would thus correspond to approximately 1 ML coverage of Au. The peak intensity is also dependent on the beam current in the storage ring as well as the measurement time of the spectra. Thus in order to do the mentioned intensity comparisons the peaks were normalized with respect to the background intensity. The measured intensity of the clean Ir surface component was $A_{Ir} = 35.5$ normalized area units. The different Au intensities, and their relation to the Ir area, can be seen in table 5.2.

[3] The XPS data suggests that 7% of the atoms are *bulk* atoms at Au coverage 0.5 ML. At an Au coverage of 1 ML 20% are bulk atoms.

[4] For more information on STM the reader is directed to the following example literature By Dawn Bonnel: Scanning Probe Microscopy and Spectroscopy: Theory, Techniques, and Applications, second Edition.

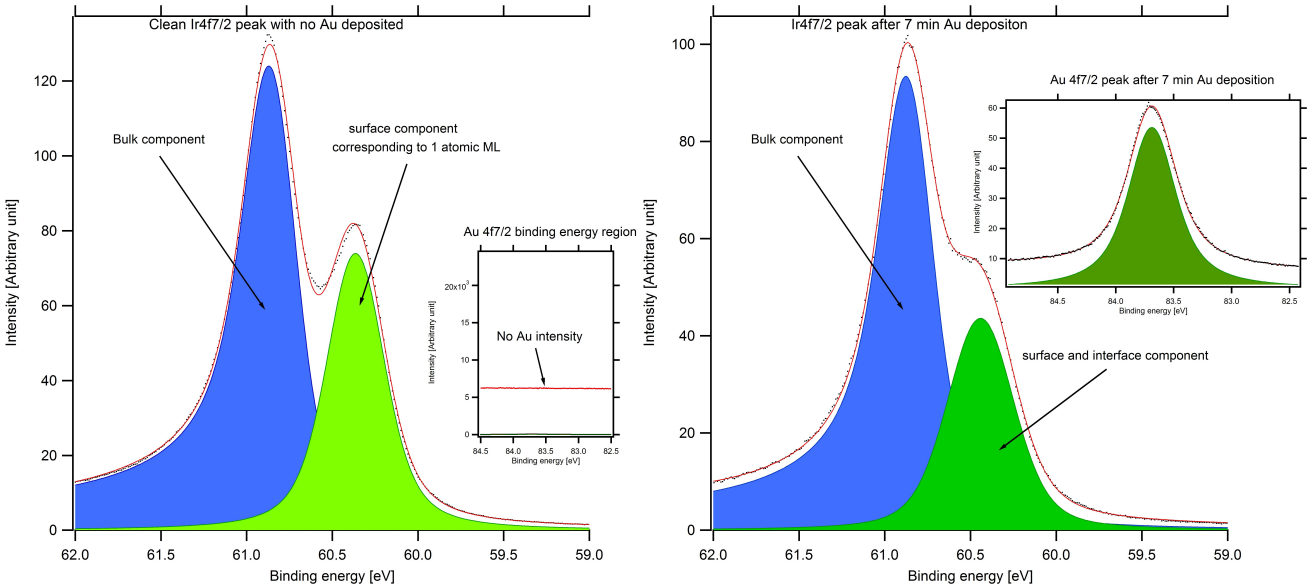

(a) no Au deposited *(b)* 7min Au deposition

Fig. 5.3: Figure (a) displays a deconvolution of the Ir$4f_{7/2}$ peak before Au deposition. The sub figure shows the Au binding energy region of the same spectra and is demonstrating that no Au is present. Figure (b) exhibits the very same Ir peak but after a 7 minute Au dose. The sub figure now indicates that Au is present though at the cost of Ir surface peak intensity. An additional surface component is present, chemically shifted slightly due to Ir-Au bonds. The shift is however very small making it appear as if only one slightly broadened surface peak is present. The Au calibration is done by relating the Au peak intensity in fig. (b) with the Ir surface component intensity in fig. (a).

This assumes that the photoemission cross section is the same for both the measured peaks, Ir $4f_{7/2}$ and Au $4f_{7/2}$. However, theoretical Cross sections calculated using the dipole length approximation [16] suggested that the cross sections differed, see table 5.1, with a factor of approximately 1.54. There is however a large error margin in the cross section values for the specific photon energy used in the experiment which makes the correction factor rather unreliable. Furthermore the photoelectrons might undergo diffraction[5] which might affect the intensity, thus making the measured intensities somewhat unreliable. In addition, the intensity normalization process has an error margin which can not be disregarded. All these factors make it extremely difficult to make an accurate calibration. In order to have a frame of reference I decided to stick with the original values, discarding any corrections, knowing that the estimated coverages will have an error margin of roughly 30-40 $\%$.

Plotting the values from the table resulted in a linear trend which indicated a cluster growth rate of approximately 0.0018 ML/s[6]. Thus a deposition time of about 550 seconds would correspond to 1 ML Au coverage.

5.4 Data and Analysis

Having calculated an appropriate Au coverage calibration curve it is possible to start analyzing the data from the XPS experiments. In order to interpret any catalytic properties of the Au clusters this section will be divided into two parts. One including the experiments on Au clusters without CO, and one including CO deposition.

[5] Due to the particle-wave duality of matter electrons might be described as waves which might undergo diffraction on the lattice constructed by the surface atoms.

[6] Note: This was calculated without the correction from the differing photoemission cross sections.

Tab. 5.1: Photoemission cross sections for Au $4f$ and Ir $4f$ at a photon energy of 200 eV.

Photonemission cross sections	
Au $4f$:	2.783 Mbarn
Ir $4f$:	4.281 Mbarn

Tab. 5.2: Putting the Au peak intensity in relation to that of the clean Ir $4f_{7/2}$, 35.5 rel. units, the Au coverage can be estimated (in units of Ir Mono layers). These estimated coverages have an error margin of about 30-40 %.

Deposition time [s]	Au relative intensity [a.u.]	Estimated Au coverage [ML]
120	6.59	0.19
420	29.33	0.83
420+240	50.47	1.42

5.4.1 Au Clusters

The deposition of Au on the Graphene film results in it constructing clusters in an ordered fashion, mainly on HCP domains of the moiré superstructure, which will grow larger as the Au dose is increased. Figure 5.4a illustrates this growth process. The spectrum shows a single well defined and broad peak after a low Au dose which narrows with increasing Au dose. However at a certain point, around 0.5 ML Au, the peak starts to be slightly asymmetric with a shoulder on the high binding energy side which is increasing in intensity with the Au dose.

This indicates that at low coverages only one layer of atoms is formed, referred to as **Au**-C *surface* atoms, see fig. 5.5. At higher coverages, approximately 0.5 ML, the Au clusters will have grown large enough to allow a second layer of atoms, enabling two new atomic species referred to as (Au)-**Au**-C *bulk* atoms and **Au**-(Au)-C *surface* atoms. The result of this is that the Au peak at low coverages will be well defined and composed only by a single component, the **Au**-C *surface* component, whilst at high coverages it will be asymmetric since it is now composed of three different components. Two representing the first and second layer *surface* atoms at lower binding energies and one representing the (Au)-**Au**-C *bulk* atoms at higher binding energies.

However, the deconvolution of the Au peak in fig. 5.4b indicated that only two components, bulk and surface, were present at high Au coverages. By estimating the binding energy difference of the two surface species to be very small this could be explained since they would thus appear to be one single component.

The binding energy of the appearing (Au)-**Au**-C *bulk* component (83.96 eV) was approximately 0.3 eV higher than that of the two surface components (83.65 eV). These binding energies as well as the energy difference correspond well to the surface (83.7 eV) and bulk (84.0 eV) components of a clean Au(111) crystal [3], supporting that the components indeed represent *surface* and *bulk* atoms.

5.4.2 Au Clusters dosed with CO

The CO dosing time was 2 minutes with a chamber pressure of 10^{-7} Torr in all experiments. The dosing temperature was approximately 105 K[7]. Higher dosing times, up to 4 minutes, did not have a noticeable effect on the CO adsorption, indicating that the Au clusters were already saturated. The low temperature was necessary since the CO molecules desorbed almost immediately at room temperature. The adsorbed CO molecules resulted in an additional component at higher BE in the Au $4f_{7/2}$ spectrum, approximately +1-1.2 eV relative to the surface component, hence referred to as the CO-Au interface component. Comparing figures before and after CO dosing, fig. 5.4a respective fig. 5.6a, clearly indicates the presence of this additional CO-Au component.

Figure 5.6b illustrates the development of each component as the Au dose is increased. At 0.2 ML Au 75%[8] of the peak intensity is represented by Au surface atoms directly related to CO molecules, leaving only 25% to be unaffected. When the Au dose is increased to 0.5 ML the portion of the Au cluster which is unaffected by CO grows considerably, and even if the the CO-Au component doubles in intensity, it now represents 46% of the total peak intensity. At 0.5 ML coverage roughly 60% of the Au surface atoms were affected by adsorbed CO molecules. At even higher coverages, 1 ML, the surface and bulk components continue to grow larger. The intensity of the CO-Au component has however decreased in comparison to lower Au coverages, only 21% of the Au surface atoms had formed bonds

[7] The system was cooled with liquid nitrogen having a boiling temperature of 77,35 K.
[8] Estimated by dividing the CO induced signal with the signal from the Au atoms unaffected by CO.

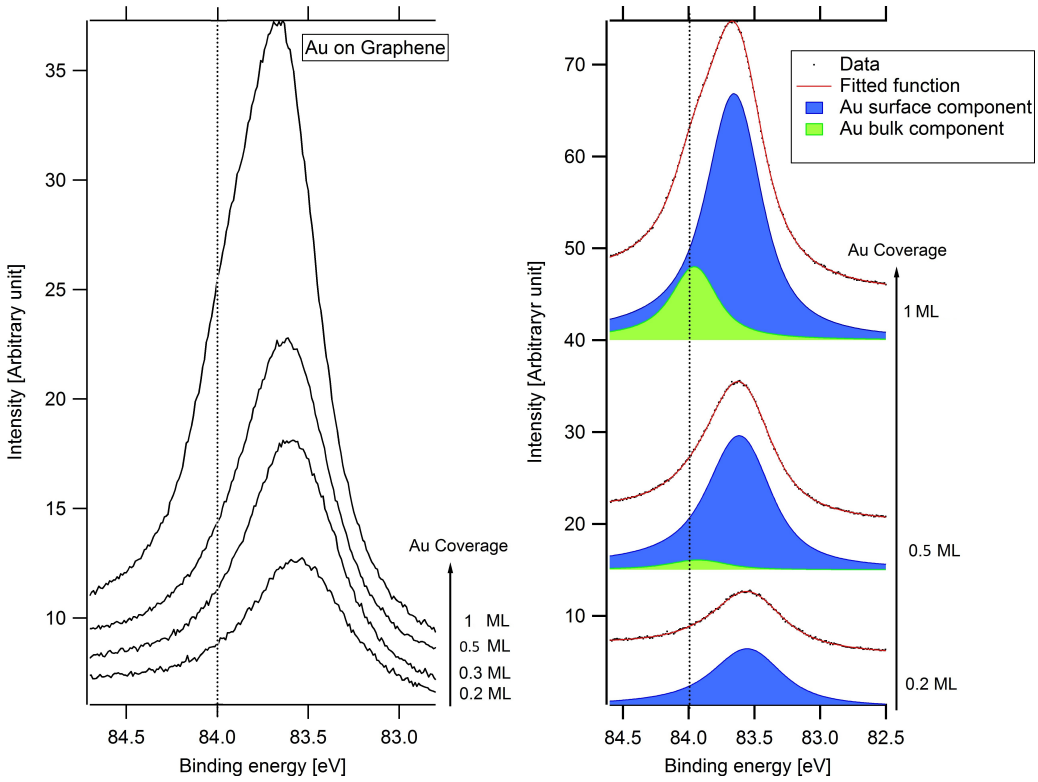

(a) Au peak data at various Au coverages

(b) Deconvolution of Au peak into surface and bulk component

Fig. 5.4: Figure (a): The spectra show a single well defined and broad peak after a low Au dose which narrows with increasing Au dose. However at a certain point, around 0.5 ML Au, the peak starts to be slightly asymmetric with a shoulder on the high binding energy side, representing *bulk* atoms, which is increasing in intensity with the Au dose. This indicates that at approximately 0.5 ML Au coverage the Au clusters starts to form a second layer. Figure (b) illustrates the deconvolution of the Au peak at different Au coverages. The dashed line, in both fig. (a) and (b), represents the BE of a bulk component of a clean Au crystal.

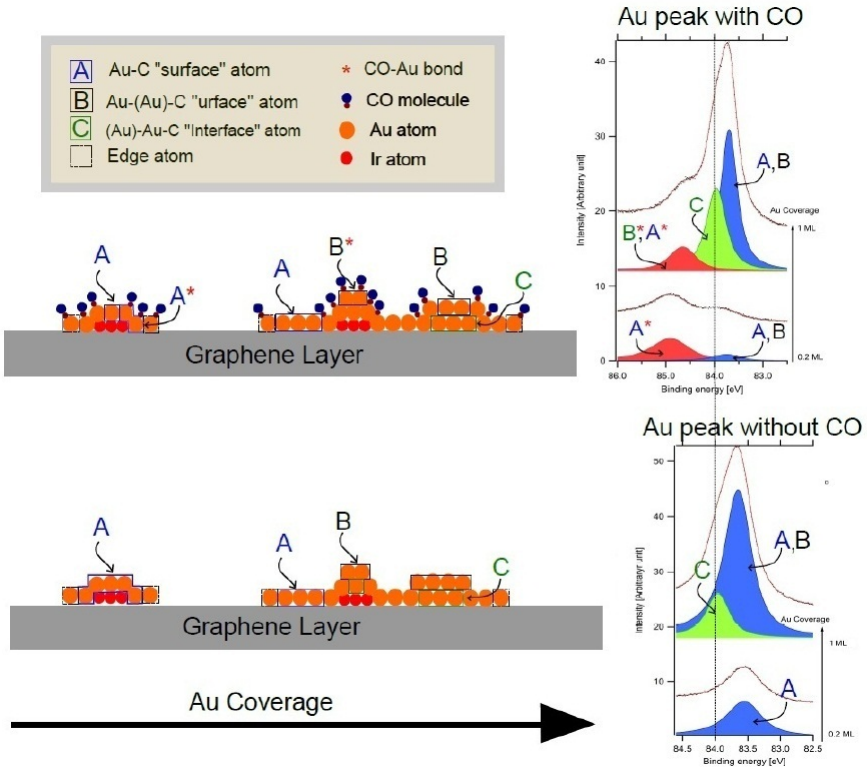

Fig. 5.5: The figure displays two different Au cluster, before and after CO deposition, and identifies the most obvious atomic species present. The different species will give rise to several different components in the Au peak, which are identified in the graphs on the right hand side. In this figure the assumption is made that the CO molecules adsorb on *edge* and *step* atoms. The red atoms represent the Ir atoms used in the seeding process and is displayed to show that the Au cluster totally covers the seeded Ir cluster. There should also be a small Ir-Au component, which is presumed to be superimposed on the surface component (blue), giving rise to a slight broadening effect.

with CO, indicating that CO adsorption is preferable on small to medium sized clusters, see table 5.3 and 5.4 for details.

Regarding BE shifts, due to the now present CO-Au atoms, of the surface and bulk atoms which had not formed bonds with CO, a shift towards higher binding energies with respect to the clean Au clusters was observed. The magnitude of the shift varied from 0.2-0.05 eV depending on cluster size. The shift was more apparent for small clusters, and the effect was slightly less noticeable for bulk atoms in comparison to surface atoms. This indicates that CO adsorption on parts of the cluster influences the electronic structure of the whole cluster, including the bulk. Figure 5.6b also displays a BE shift, approximately 0.25 eV, of the CO-Au component towards lower binding energies with increasing Au cluster size. This suggests that different CO-Au species exist depending on the Au cluster size.

Also noticed was that the intensity of the surface component decreased when CO was adsorbed on the surface. But the intensity loss was not totally covered by the intensity of the appearing CO-Au component as would be expected. Instead the bulk component seemed to have increased in size, being 60-80% larger then before the CO dose. This effect was larger for smaller clusters. This suggests that the adsorption of CO molecules reorganizes the Au cluster structure so that more underlying bulk atoms now are present. This is however unlikely at the low temperatures used. An other possibility is the diffraction phenomenom, mentioned in section 5.3.1, which migh increase the intensity of the bulk atoms. This in conjunction with errors in the fitting and normalization process might explain the increase of bulk intensity.

It might also be of interest to determine the type of Au atoms that the CO molecules prefer to bind to. The oxygen spectrum in fig. 5.7 suggests that several oxygen species are present which in turn means that several adsorption sites

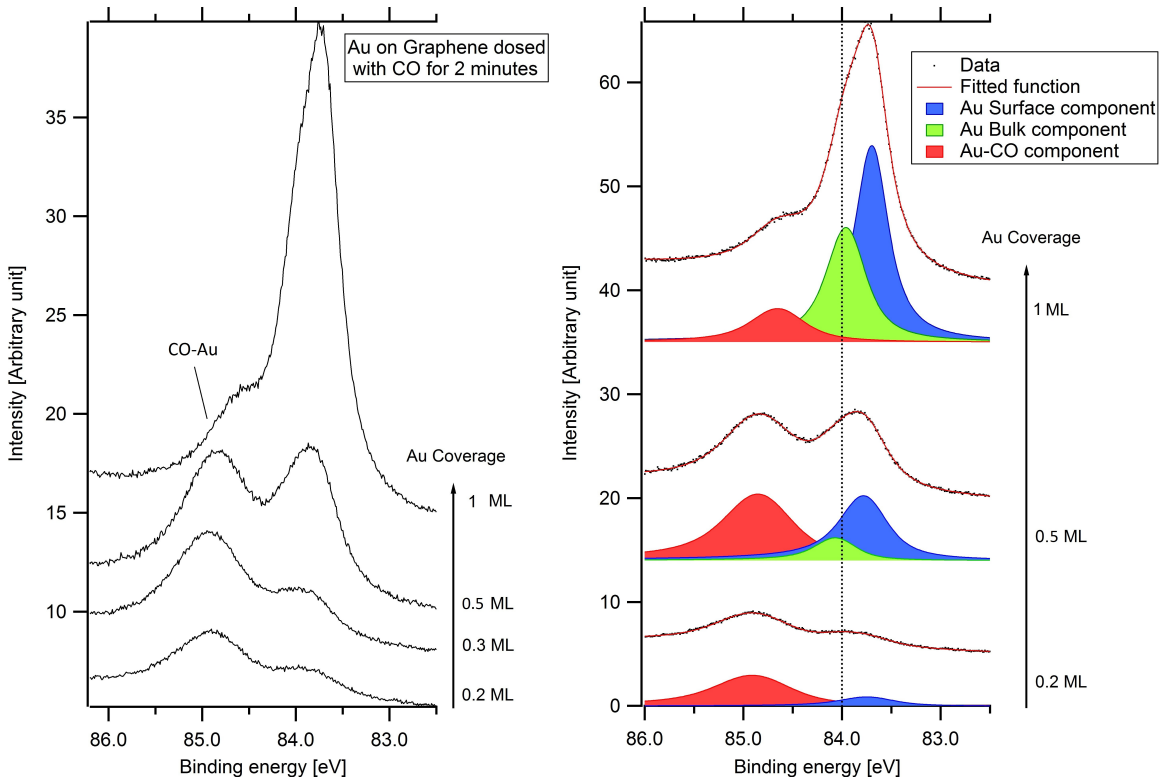

(a) Au peak data after CO dosing at various Au coverages.

(b) Deconvolution of Au peak after CO dosing.

Fig. 5.6: Figure (a) displays the development of the Au4$f_{7/2}$ peak as the Au coverage increases after 2 minutes of CO exposure. A new component at higher binding energies is now present, representing Au atoms bonded to a CO molecule. Figure (b) displays the deconvolution of the Au peak, dividing it up into three components. The bulk and surface components, as before the CO deposition, and the new CO-Au component. The intensity of the CO-Au component seems to increase up until it reaches 0.5 ML Au coverage, at which it starts to decrease. This indicates that the size of the Au clusters plays a very important role in the adsorption of CO. The dashed line represents the BE of a bulk component of a clean Au crystal.

are preferable on the Au cluster. The present species also seem to change as the Au cluster grows larger. At low Au coverages, 0.2 ML, most of the intensity is represented by the CO-Au component, meaning that almost all surface atoms, roughly 75%, of the Au cluster is involved in a CO bond. At such small coverages the cluster is probably irregular and a great portion of the cluster is represented by edge atoms. Thus indicating that edge atoms are popular CO adsorption sites.

However larger clusters should have even more edge atoms and thus more CO-edge bonds. The doubling of CO induced intensity for 0.5 ML clusters supports this. The CO induced intensity of the 1 ML cluster is however much smaller, indicating that more than just edge atoms are involved, an assumption supported by the oxygen spectrum. The larger clusters ,0.5-1 ML, should consist of at least 2-3 atomic layers and should thus have many *corners* and *steps*. Assuming that also steps are favorable adsorption sites the presence of such could explain the increase in CO adsorption for the 0.5 ML cluster as well as the decrease for the 1 ML cluster. The larger cluster, having twice the amount of atoms, might consist of more "complete" atomic layers than the smaller one, and thus having larger terasses but lesser steps.

Thus the medium sized clusters, around 0.5 ML, appear to have the largest number of adsorption sites since it has second layer atoms giving rise to steps, while still consisting of a relatively large amount of edge atoms. This theory is supported by similar findings regarding Au cluster adsorption sites in [3]. Those clusters were however grown on a totally different substrate, CeO_2, but the fundamentals of the cluster properties might still be comparable.

Tab. 5.3: Displaying how the relative intensity of the CO-Au component changes with the Au coverage, in addition the BE shift of the CO-Au component is also shown.

Au coverage [ML]	CO-Au intensity	CO-Au BE [eV]
0.2	1.00	84.90
0.5	2.02	84.85
1	0.79	84.65

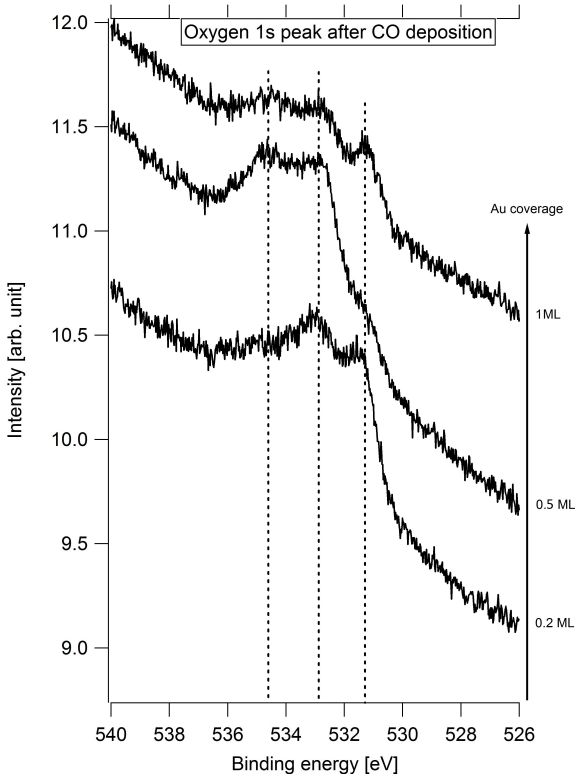

Figure 5.7: The figure displays the oxygen 1s peak at various Au coverages. There appears to be a number of oxygen species present as the peak appearance is very distorted. Certain species seem to be more abundant at lower Au coverages, and some at higher coverages, indicating several preferable adsorption sites for the CO molecule on the Au cluster.

Tab. 5.4: Displaying how the relative intensity of the CO-Au component changes with the Au coverage, in addition the BE shift of the CO-Au component is also shown.

Au Coverage [ML]	Surface intensity [a.u]	Bulk intensity [a.u]	CO-Au intensity [a.u]	Total intensity [a.u]	Fraction of Bulk atoms	Fraction of surface atoms involved with CO
Before Co deposition						
0.2	1,61	-	-	1.61	-	-
0.5	3.20	0.21	-	3.43	7%	-
1	5.21	1.31	-	6.52	20%	-
After Co deposition						
0.2	0.32	-	1.00	1.32	-	75%
0.5	1.37	0.39	2.02	3.79	10%	60%
1	3.07	2.02	0.79	5.88	34%	21%

5.5 Results from XPS

The XPS data suggests that the Au clusters have a *stepwise* growth and that they entirely cover the seeded Ir atoms, except for extremely small Au coverages. An Au coverage of 0.5 ML appear to be the threshold for inducing growth of a second layer of the Au cluster. Higher coverages clearly indicate the presence of second, and possibly third, layer atoms by the two extra components that are present in the spectrum. The binding energies of both components correspond well to those of bulk and surface atoms of a clean Au crystal.

Exposure to CO gives rise to an additional component in the Au spectrum, at +1-1.2 eV relative to the surface component. This component is represented by Au atoms that are in direct contact with a CO molecule. The intensity variations with respect to cluster size of this component suggests that mid sized, 0.5 ML, clusters have the largest number of adsorption sites. In these clusters about 60 % of the Au surface atoms were chemically active. The chemically active atoms were "identified" as *corner* atoms and *step* atoms, since a large number of steps/corner atoms are expected in 0.5 ML clusters. This conclusion is supported by similar findings in [3]

A shift of +0.2-0.05 eV, depending on cluster size, of all the Au components was noticeable when CO was adsorbed. Thus indicating the CO adsorption influences the electronic structure of the whole cluster, even the bulk.

The data also indicated that the bulk component of the Au cluster became larger when CO was deposited. This indicates that a reconstruction of the cluster due to CO adsorption occurred. The reliability of this result is questionable since the temperatures are very low. Thus large error margins or diffraction phenomena are more probable causes.

6. SUMMARY

In summary CO adsorption on Au clusters have been studied using XPS. The substrate was an Ir(111) crystal covered by a monolayer of Graphene, giving rise to a super lattice. The Graphene surface had a wavelike structure, with super structure lattice points at each minimum, posing as preferable Au adsorption sites. This was investigated using LEED. The distance between these adsorption sites, 25 ± 2 Å and 26 ± 4 Å, as well as the Graphene lattice constant, 2.46 ± 0.03 Å, was calculated using known values of the Ir lattice constant as a reference.

In order to grow the Au clusters, seeding with Ir atoms was necessary. The clusters appeared to grow in a stepwise fashion, not finishing the first atomic layer before growth of the second one was initiated. The size of the Au clusters in terms of monolayers (ML) were estimated, but with a larger error margin since the process was difficult without the use of STM. The relative size between the clusters should however be precise.

The experiments indicated that medium sized clusters were optimal regarding CO adsorption. Up to 60 $\%$ of the surface atoms of these clusters were chemically active. The atoms of larger clusters were mostly inactive, only about 20 $\%$ of them were bonded to CO.

Regarding the XPS results, more measurements would be preferable to further support the results and conclusions made. Only a few spectra with different Au coverages were taken, making the statistics somewhat unreliable. However, correlations between these results and similar studies suggests that they still are reliable.

7. ACKNOWLEDGMENTS

I would like to extent my sincere thanks to my supervisors Jesper N. Andersen and Jan Knudsen for their genuine support and help during this Bachelor project. In particular I would like to express my appreciation for the many rewarding discussions we have had, and for using their limited time to answer my endless stream questions, as it is those discussions and answers that defines the final result of this thesis.

In addition I would also like to thank Elin Grånäs and Sara Blomberg for exchanging many novel ideas with me, and helping me puzzle some of the pieces together.

BIBLIOGRAPHY

[1] M. Haruta, T. Kobayashi, H. Sano, and N. Yamada *Chemical letters*, vol. 2, pp. 405–408, 1987.

[2] E. D. Park and J. S. Lee, "Effects of pretreatment conditions on co oxidation over supported au catalysts," *Journal of Catalysis*, vol. 186, pp. 1–11, August 1999.

[3] C. J. Weststrate, A. Resta, R. Westerstro1m, E. Lundgren, A. Mikkelsen, and J. N. Andersen, "Co adsorption on a au/ceo$_2$ (111) model catalyst," *Journal of Physical Chemestry*, vol. 112, pp. 6900–6906, February 2008.

[4] P. Hofmann, "Lecture notes on surface science." `http://www.philiphofmann.net/surflec/surflec.html`. [Online; accessed 2010-05-13].

[5] G. Attard and C. Barnes, *Surfaces*. New York: Oxford University Press, 1998.

[6] G. Ertl and J. Kuppers, *Low Energy Electrons and Surface Chemistry*, ch. 9, pp. 201–227. Vch Pub, 2 ed., March 1986.

[7] J. Gustavsson, "Physics and chemistry of surfaces; surface diffraction." `http://www.sljus.lu.se/staff/anders/diffraction.pdf`, 2010. [Lecture Handout].

[8] A. T. N'Diaye, J. Coraux, T. N. Plasa, C. Busse, and T. Michely, "Structure of epitaxial graphene on ir(111)," *New Journal of Physics*, vol. 10, p. 043033, April 2008.

[9] A. N'Diaye, T. Gerber, C. Busse, J. Myslivecek, J. Coraux, and T. Michely, "A versatile fabrication method for cluster superlattices," *New Journal of Physics*, vol. 11, p. 103045, October 2009.

[10] A. N'Diaye, S. Bleikamp, P. J. Fiebelman, and T. Michely, "Two-dimensional ir cluster lattice on a graphene moir*é* on ir(111)," *Physical Review Letters*, vol. 97, p. 215501, November 2006.

[11] J. Wintterlin and M.-L. Bocquet, "Graphene on metal surfaces," *Surface science*, vol. 603, pp. 1841–1852, January 2009.

[12] F. W. Sears, M. W. Zemansky, and H. D. Young, *University Physics*, pp. 843–4. Addison-Wesley, 6 ed., 1983.

[13] R. Macovez, *Surface electronic structure of fullerides*. PhD thesis, University of Groningen, 2007.

[14] R. van Gastel, A. N'Diaye, D. Wall, J. Coraux, C. Busse, F.-J. M. zu Heringdorf, N. Buckanie, M. H. von Hoegen, T. Michely, and B. Poelsema, "Selecting a single orientation for millimeter sized graphene sheets," *Applied physics letters*, vol. 95, pp. 121901–121901–3, July 2009.

[15] J. Coraux, A. T. N'Diaye, M. Engler, C. Busse, D. Wall, N. Buckanie, F.-J. M. zu Heringdorf, R. van Gastel, B. Poelsema, and T. Michely, "Growth of graphene on ir(111)," *New Journal of Physics*, vol. 11, p. 023006 (22pp), February 2009.

[16] J. Yeh and I.Lindau, "Atomic data and nuclear data tables." `http://ulisse.elettra.trieste.it/services/elements/WebElements.html`, 1985. [Online; accessed 2010-08-12].